Earthquake Science
地震学报英文版 ISSN 1674-4519 CN 11-5695/P

Rayleigh wave waveform-amplitude spectrum joint inversion: an advanced resolution-stability approach for loess near-surface imaging

Keyu Huo, Guangzhou Shao, Jing Hu, Hua Wu, Guoshun Wang, Weishuai Chang, Pengqi Wang

Citation: Huo K, Shao GZ, Hu J, Wu H, Wang GS, Chang WS, Wang PQ (2026). Rayleigh wave waveform–amplitude spectrum joint inversion: an advanced resolution–stability approach for loess near–surface imaging. *Earthquake Science*, **39**(0): 1–23, doi:

View online:

Related articles that may interest you

Earthquake Science 39 (2026) 1–23

Contents lists available at ScienceDirect

Earthquake Science

Journal homepage: https://www.keaipublishing.com/en/journals/earthquake-science/

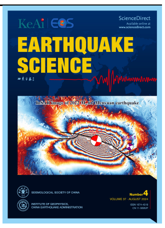

Rayleigh wave waveform-amplitude spectrum joint inversion: an advanced resolution-stability approach for loess near-surface imaging

Keyu Huo[1], Guangzhou Shao[1,✉], Jing Hu[1,✉], Hua Wu[2], Guoshun Wang[3], Weishuai Chang[1] and Pengqi Wang[1]

[1] *School of Geological Engineering and Geomatics*, *Chang'an University*, *Xi'an*, 710054, *China*
[2] *School of Science*, *Chang'an University*, *Xi'an*, 710064, *China*
[3] *China Water Resources Beifang Investigation*, *Design and Research Co. Ltd.*, *Tianjin*, 300222, *China*

Key points:

- A joint inversion method integrating Rayleigh wave waveform and amplitude spectrum is proposed to tackle limitations of conventional inversion in loess near-surface exploration, including low lateral resolution, strong dependence on initial models and proneness to converging to local minima.
- A dynamically weighted joint objective function is designed: amplitude spectrum inversion is prioritized in the early stage to construct stable background models, while the weight of waveform inversion is gradually increased in the later stage to improve resolution.
- Numerical simulations show the joint method outperforms single waveform/amplitude spectrum inversion in 2D shear-wave velocity inversion, with higher stability/accuracy for characterizing concealed geological defects.
- Low-frequency constraints from amplitude spectrum inversion reduce initial model dependence; RMSE fluctuation is only 7.0%, far lower than 31.6% of conventional waveform inversion.
- Field application in Taibai loess area (Shaanxi) achieves high-resolution imaging of 0–20 m subsurface structures, accurately locating tunnels and providing engineering safety support.

ABSTRACT

Rayleigh wave methods are widely utilized in near-surface geophysical exploration within loess regions. However, conventional dispersion curve inversion methods are constrained by the horizontally layered media assumption, which restricts their lateral resolution and prevents the identification of collapsible voids, hidden faults, and other concealed defects. With advances in computational power, wave-equation-based waveform inversion and amplitude spectrum inversion have emerged as promising

Production and Hosting by Elsevier on behalf of KeAi

Peer review under the responsibility of Institute of Geophysics, China Earthquake Administration.

✉ **Corresponding author.** Shao GZ, email: shao_gz@chd.edu.cn; Hu J, email: hujing@chd.edu.cn

Article history:

https://doi.org/

techniques for characterizing shallow subsurface structures. Nevertheless, waveform inversion often converges to local minima due to insufficient low-frequency components and a strong dependence on the initial model. Although amplitude spectrum inversion can partially alleviate these issues by exploiting low-frequency Rayleigh waves, it neglects the critical role of high-frequency waveform components and the effective use of single-trace data in improving inversion resolution. To address these limitations, this study proposes a joint inversion method that integrates the Rayleigh wave amplitude spectrum with full waveform data. A joint objective function with dynamically variable weights is constructed. By dynamically adjusting the relative weights of the two components during the iteration process, amplitude spectrum inversion is prioritized in the early stages to build a stable background velocity model and mitigate cycle-skipping problems. In later stages, the weight of waveform inversion is gradually increased to leverage high-frequency information for improving model resolution. This strategy simultaneously compensates for the shortcomings of each individual approach and enhances convergence efficiency. Numerical simulation results demonstrate that compared with conventional individual waveform inversion or amplitude spectrum inversion, the proposed joint inversion method achieves higher accuracy and stability in 2D shear-wave velocity inversion. Furthermore, field data applications from the loess area substantiate the practical value of this method in engineering-scale near-surface exploration.

Keywords: Waveform Inversion; Amplitude Spectrum Inversion; Joint Inversion; Objective Function; Near-surface Exploration

Citation: Huo K, Shao GZ, Hu J, Wu H, Wang GS, Chang WS and Wang PQ (2026). Rayleigh wave waveform-amplitude spectrum joint inversion: an advanced resolution-stability approach for loess near-surface imaging. Earthq Sci **39**, doi:

1. Introduction

The Loess Plateau is a vital base in China for energy, industrial, and agricultural production, as well as a crucial economic corridor connecting northwest China with Central Asia and Europe under the Belt and Road Initiative. However, due to unique physical properties such as a loose structure and strong collapsibility, loess is highly susceptible to erosion. This vulnerability leads to the widespread formation of concealed geological defects, including collapsible sinkholes and ground subsidence. Frequent geological hazards pose significant threats to civil engineering projects in western loess regions, necessitating the accurate detection of their distribution and scale. Geophysical exploration provides economical, rapid, and non-destructive methods for this purpose. Among these, seismic exploration offers relatively high resolution and accuracy, but is limited by the complex geological conditions of loess areas. The loess overburden typically possesses a loose, porous structure containing significant amounts of gas and unsaturated water. The interaction between pore fluids and the solid matrix leads to rapid attenuation of high-frequency energy and strong scattering effects. While these conditions severely degrade the signal-to-noise ratio of reflection seismic data, surface wave exploration centered on Rayleigh waves has gradually become a research hotspot due to its adaptability to the well-developed surface wave characteristics in loess regions. In near-surface seismic wavefields, the Rayleigh wave is the dominant wave type, accounting for up to 67% of the total wavefield energy and exhibiting a higher signal-to-noise ratio than body waves (Socco et al., 2010; Woods, 1968). The dispersion characteristics of Rayleigh waves serve as a proxy for shear-wave velocity variations within subsurface media (Chen YQ and Saygin, 2022; Le Z et al., 2024; Tran and Hiltunen, 2012; Wang J and Yan YF, 2021; Xue YH et al., 2024). Owing to these properties, Rayleigh wave methods offer distinct advantages for near-surface geological surveys (Song ZH et al., 2021; Wu YH et al., 2023). Conventional Rayleigh wave methods – such as Multichannel Analysis of Surface Waves (Park et al., 1999; Park, 2013), Ambient Noise Imaging (Chang WS et al., 2025; Huo KY et al., 2023; Wang CF et al., 2014; Wang XN et al., 2022; Weemstra et al., 2013) typically rely on a horizontally layered media assumption. These methods estimate 1D vertical velocity profiles by inverting dispersion curves. Consequently, they exhibit pronounced limitations in applicability when encountering geological conditions with lateral velocity variations (Mi BB et al., 2017).

To address the bottleneck of low lateral resolution in dispersion curve inversion, researchers have turned their focus to wave-equation-based inversion methods, which directly utilize the full-waveform information of seismic signals to reconstruct subsurface structures, thereby circumventing the constraints of the layered medium assumption. Tarantola introduced full waveform inversion (FWI), which reconstructs subsurface structures by minimizing the residuals between observed and modeled seismic waveforms (Tarantola, 1984). Theoretically, FWI utilizes the information of all wave types in the seismic records. By bypassing intermediate operations such as dispersion curve extraction, it provides a highly promising solution for the accurate reconstruction of the near-surface model (Gao LL et al., 2023; Lamuraglia et al., 2023; Long GH et al., 2009; Pan YD et al., 2018, 2019; Tohti et al., 2022; Yilmaz et al., 2022). Zeng et al. demonstrated the feasibility of obtaining shallow shear-wave velocities through Rayleigh wave waveform inversion (Zeng C et al., 2011). Tran and McVay successfully performed time-domain elastic full waveform inversion using synthetic surface wave records and field data within the 20 Hz frequency range, achieving accurate imaging of subsurface structures at depths shallower than 20 meters (Tran and McVay, 2012). Pan et al. accomplished time-domain Love wave waveform inversion (Pan YD et al., 2016). Wittkamp et al. showed that joint inversion of Rayleigh and Love wave waveforms can significantly improve near-surface imaging resolution (Wittkamp et al., 2019). Groos et al. developed a comprehensive workflow for two-dimensional elastic full waveform inversion and applied it to field-acquired Rayleigh wave data (Groos et al., 2017). Although FWI theoretically possesses the potential to overcome the lateral resolution limitations of conventional surface wave methods, its inherent high nonlinearity and non-convex objective function present significant challenges (Espin et al., 2023; Operto et al., 2023; Xie C et al., 2024). When initiated with inaccurate starting models, cycle-skipping phenomena may occur during FWI optimization, causing the inversion to converge to local minima. This issue is particularly pronounced in loess areas, which are frequently characterized by strong lateral heterogeneity, such as sinkholes, vertical joints, and hidden engineering defects. The complex wavefield scattering caused by these features makes pure FWI highly nonlinear and prone to cycle-skipping, thereby limiting its practical application. To effectively mitigate cycle-skipping issues and reduce the initial model sensitivity, Bunks et al. proposed a time-domain multi-scale inversion strategy (Bunks et al., 1995). This approach sequentially inverts from low to high frequencies, using the low-frequency inversion results as the initial model for subsequent frequency bands. This strategy reduces the nonlinearity of the inverse problem and ultimately enables accurate full-frequency-band wavefield reconstruction (Virieux and Operto, 2009; Yuan et al., 2015; Fichtner et al., 2024). Borisov et al. further demonstrated that envelope-based objective functions can effectively resolve large-scale shallow heterogeneities while mitigating cycle-skipping problems, with surface waves providing robust constraints on complex near-surface properties (Borisov et al., 2018).

To further alleviate the nonlinearity issues of waveform inversion, amplitude spectrum inversion and dispersion spectrum inversion have been proposed as complementary techniques and demonstrated unique advantages. Li et al. proposed the wave-equation dispersion inversion method, also termed “skeleton inversion,” which utilizes Rayleigh wave phase velocity information rather than full waveform data, thereby providing more robust convergence for the final velocity model (Li J et al., 2017, 2019a, b). Pérez and Masoni et al. developed a windowed amplitude waveform inversion approach that employs the frequency-wavenumber (f-k) spectrum of seismic signals as the objective function, effectively reducing local minima in the optimization process (Masoni et al., 2014; Pérez et al., 2014). Dal Moro et al. implemented a full velocity spectrum multicomponent surface wave inversion strategy that significantly decreased solution non-uniqueness while improving stability (Dal Moro et al., 2015). Pan and Innanen demonstrated that amplitude-based misfit functions exhibit enhanced sensitivity to attenuation anomalies (Pan WY and Innanen, 2019). Hu et al. introduced a multistage phase-correction elastic FWI method in the frequency-wavenumber domain, verifying its effectiveness in mitigating cycle-skipping risks through Marmousi model tests (Hu Y et al., 2022). Zhang et al. revealed that dispersion-spectrum-based objective functions eliminate the need for dispersion curve picking while maintaining relatively low ill-posedness in inverse problems (Zhang ZD et al., 2020, 2021, 2024). Pan et al. developed a stochastic objective function approach for near-surface inversion, where the f-k dispersion spectrum serves as an essential component (Pan YD et al., 2021; Pan YD and Gao LL, 2023). These studies collectively demonstrate that f-k domain dispersion amplitude spectrum objective functions not only adapt to various geological scales for S-wave velocity inversion but also exhibit remarkable reliability in field data applications, suggesting broad engineering potential. However, since these methods primarily utilize energy information while neglecting phase details, they often suffer from limited resolution, resulting in insufficient accuracy for characterizing fine-scale subsurface structures compared to full waveform inversion.

Notably, current implementation schemes for near-surface full-waveform inversion mainly adopt either waveform misfit or amplitude spectrum misfit alone as the objective function. Given the complementary advantages and inherent limitations of waveform inversion and amplitude spectrum inversion, integrating these two methods to construct a joint inversion framework can avoid the methodological and technical limitations of conventional reflection wave methods and surface wave methods in the loess area, and compensate for the lack of low-frequency information in body-wave waveform inversion. Therefore, a joint inversion strategy that combines the stability of the amplitude spectrum with the resolution of waveforms is essential for accurate imaging in this specific geological environment.

To bridge this methodological gap, this study proposes a joint inversion method of Rayleigh wave waveform and amplitude spectrum. The core idea of this method is to design a hybrid objective function that simultaneously incorporates waveform misfit and amplitude spectrum misfit. By dynamically adjusting the weighting coefficients of the two misfit terms during the inversion iteration process, the method fully exploits the low-frequency constraint advantage of amplitude spectrum inversion and the high-resolution imaging capability of waveform inversion. This integration not only improves the convergence stability of the inversion process but also enhances the resolution of the inverted shear-wave velocity model.

The remainder of this paper is structured as follows: Section 2 provides a comprehensive presentation of our proposed joint inversion method for near-surface Rayleigh waves, detailing the formulation of the combined amplitude spectrum and waveform objective function and the complete implementation workflow. Section 3 presents a validation conducted through both numerical simulations and field data experiments in a loess area, offering a quantitative assessment of the method's imaging performance. Section 4 presents discussion of the experimental results, including comparative analysis with conventional techniques and examination of practical implementation considerations. Finally, we conclude with a summary of key findings and contributions.

2. Methods

2.1. Formulation of Joint Objective Function and Gradient Derivation

The fundamental goal of Rayleigh wave waveform inversion is to achieve high-resolution imaging of subsurface medium parameters by minimizing the discrepancy between observed and synthetic seismic data. In conventional time-domain waveform inversion, the L2-norm objective function is commonly employed, which is mathematically expressed as follows:

$$E_1(m)=\frac{1}{2}(u_{\text{mod}}-u_{\text{obs}})\times(u_{\text{mod}}-u_{\text{obs}})^{\mathrm{T}}=\frac{1}{2}\int_t\sum_{nr}\sum_{ns}\Delta u^2(x_r,x_s,t)\,\mathrm{d}t \tag{1}$$

where u_{obs} is the observed seismic data, u_{mod} is the synthetic seismic data, m is the model parameter corresponding to the synthetic seismic data; Δu is the wavefield residual, the superscript T represents the matrix transpose operation, ns is the number of shots, and nr is the number of traces, $u(x_r,x_s,t)$ is the wavefield at the time step t and the positon x_r and x_s.

The amplitude spectrum of Rayleigh waves plays a critical role in waveform inversion owing to its distinctive physical characteristics. In near-surface wavefields, Rayleigh waves naturally dominate the recorded energy and exhibit lower frequencies compared to body waves (Socco et al., 2010). Specifically, by minimizing the residual of the amplitude spectrum in the F-K domain, the method focuses on fitting the energy distribution of the seismic signal rather than the rapid phase oscillations. This allows it to effectively retrieving the low-wavenumber background structure while partially filtering out interference from high-frequency reflected and scattered waves.

Building upon the classical time-domain objective function, the objective function for the amplitude spectrum in the frequency-wavenumber (f-k) domain can be formulated as:

$$E_2(m)=\frac{1}{2}(|U_{\text{mod}}|-|U_{\text{obs}}|)\times(|U_{\text{mod}}|-|U_{obs}|)^{\mathrm{T}}=\frac{1}{2}\sum_{ns}\int_f\int_k|\Delta U|^2(f,k)\,\mathrm{d}f\mathrm{d}k \tag{2}$$

where U_{mod} and U_{obs} are the f-k spectra obtained after performing two-dimensional Fourier transforms on u_{mod} and u_{obs} respectively, $|\cdot|$ denotes taking the amplitude.

By leveraging these inherent advantages of the f-k domain amplitude spectrum, this study constructs a joint objective function that integrates the Rayleigh wave amplitude spectrum (in the f-k domain) with conventional waveform data. A critical consideration in this integration is the order-of-magnitude difference in mismatch values between Rayleigh wave waveforms and the f-k domain amplitude spectrum. To eliminate the bias caused by this magnitude discrepancy, the joint objective function is established using the weighted sum of normalized objective functions from the individual Rayleigh wave waveform and amplitude spectrum. This design not only effectively tackles the strong nonlinearity inherent in the inversion process but also alleviates the cycle-skipping problem that frequently afflicts traditional waveform inversion. Within the inversion workflow, priority is given to amplitude spectrum information for constructing a robust background velocity model that fully leverages the stability of amplitude spectrum in processing low-frequency components. Once the background model is established, higher-frequency waveform components are gradually incorporated to further enhance the resolution of the inverted velocity model.

After referring to and simplifying the joint objective function proposed by Song et al. (Song C et al., 2023), we formulated the joint objective function used in this study as follows:

$$E(m)=\frac{1}{2}(1-\omega)\|\frac{|U_{mod}|}{\||U_{\mathrm{mod}}|\|_2}-\frac{|U_{obs}|}{\||U_{\mathrm{obs}}|\|_2}\|_2^2+\frac{\omega}{2}\|\frac{u_{\mathrm{mod}}}{\|u_{mod}\|_2}-\frac{u_{obs}}{\|u_{obs}\|_2}\|_2^2=\frac{1}{2}(1-\omega)\|\overline{|U_{mod}|}-\overline{|U_{obs}|}\|_2^2+\frac{\omega}{2}\|\overline{u_{mod}}-\overline{u_{obs}}\|_2^2=$$
$$\frac{1}{2}(1-\omega)\overline{E_2(\mathrm{m})}+\frac{\omega}{2}\overline{E_1(m)} \tag{3}$$

where ω is the dynamic weight factor, $\omega\in[0,1]$. Initially, ω is set to 0 at the beginning of the inversion process and gradually increases as the iterations proceed. Additionally, when the residual of the amplitude spectrum inversion converges to a preset threshold, the growth rate of $\omega$is accelerated to initiate waveform inversion in advance. $\overline{|U_{\mathrm{mod}}|}$ and $\overline{|U_{\mathrm{obs}}|}$ represent the normalized amplitude spectrum of the synthetic and observed wavefields, respectively. Similarly, $\overline{u_{\mathrm{mod}}}$ and $\overline{u_{\mathrm{obs}}}$ denote the normalized synthetic and observed wavefields, respectively.$\overline{E_1(m)}$ and $\overline{E_2(m)}$ represent the normalized objective function of the waveform inversion and amplitude spectrum inversion, respectively.

The dynamic weighting strategy addresses the cycle-skipping challenge through a two-stage mechanism. In early iterations, the amplitude spectrum component smooths the non-convex objective function landscape, broadening the basin of attraction around the global minimum and preventing convergence to local minima. Subsequently, the waveform component refines this globally optimal solution to achieve high-resolution accuracy. This approach enables the joint inversion to paradoxically achieve superior waveform matching compared to pure waveform inversion, as the refinement occurs at the global rather than local minimum.

During the inversion process, joint inversion efficiently computes the gradient of the objective function using the adjoint-state method, which involves calculating the zero-lag cross-correlation between the time derivative of the forward-propagated wavefield and the adjoint wavefield (i.e., the back-propagated residual wavefield) (Plessix, 2006).

First, the partial derivatives of $\overline{E_1(m)}$ and $\overline{E_2(m)}$ with respect to the model parameters m are computed separately:

$$\frac{\partial\overline{E_1(m)}}{\partial m}=\sum_{ns}\iint Re\{\overline{\Delta U}[(\nabla_{\mathrm{m}}|U_{\mathrm{mod}}|)\||U_{\mathrm{mod}}|\|_2-|U_{mod}|(\nabla_{\mathrm{m}}\||U_{\mathrm{mod}}|\|_2)]/\||U_{mod}|\|_2^2\}\mathrm{d}f\mathrm{d}k \tag{4}$$

$$\nabla_m\|U_{\mathrm{mod}}\|_2=\frac{\iint|U_{\mathrm{mod}}|\cdot\nabla_m|U_{\mathrm{mod}}|\mathrm{d}f\mathrm{d}k}{\|U_{\mathrm{mod}}\|_2} \tag{5}$$

Further simplification yields the following expression:

$$\frac{\partial\overline{E_1(m)}}{\partial m}=\sum_{ns}\iint\mathrm{Re}\left\{\overline{\Delta U}\left(\frac{(\nabla_m|U_{mod}|)}{\||U_{mod}|\|_2}-\frac{|U_{mod}|\cdot\iint|U_{mod}|\cdot\nabla_m|U_{mod}|\mathrm{d}f\mathrm{d}k}{\||U_{mod}|\|_2^3}\right)\right\}\mathrm{d}f\mathrm{d}k=$$
$$\sum_{ns}\iint\mathrm{Re}\left\{\overline{\Delta U}\left(\frac{1}{\||U_{\mathrm{mod}}|\|_2}-\frac{|U_{\mathrm{mod}}|\cdot\iint|U_{\mathrm{mod}}|\mathrm{d}f\mathrm{d}k}{\||U_{mod}|\|_2^3}\right)(\nabla_m|U_{\mathrm{mod}}|)\right\}\mathrm{d}f\mathrm{d}k$$
$$\sum_{ns}\iint\mathrm{Re}\frac{1}{\||U_{\mathrm{mod}}|\|_2}[\left(\overline{\Delta U}-\frac{|U_{mod}|\cdot\iint\overline{\Delta U}\cdot\frac{|U_{mod}|}{\||U_{mod}|\|_2}\mathrm{d}fdk}{\||U_{mod}|\|_2}\right)(\nabla_m|U_{mod}|)]df\mathrm{d}k \tag{6}$$

Similarly, the gradient of the amplitude spectrum objective function term can be derived as:

$$\frac{\partial\overline{E_2(m)}}{\partial m}=\sum_{ns}\iint\left[\frac{1}{\|u_{\mathrm{mod}}\|_2}\left(\overline{\Delta u}-\frac{u_{\mathrm{mod}}\iint\overline{\Delta u}\frac{u_{\mathrm{mod}}}{\|u_{mod}\|_2}\mathrm{d}f\mathrm{d}k}{\|u_{\mathrm{mod}}\|_2}\right)\right](\nabla_{\mathrm{m}}u_{\mathrm{mod}})\mathrm{d}x\mathrm{d}t \tag{7}$$

where $\overline{\Delta U}=\overline{|U_{\mathrm{mod}}|}-\overline{|U_{\mathrm{obs}}|}$ denotes the residual between the normalized amplitude spectrum of the synthetic and observed wavefields, and $\overline{\Delta u}=\overline{u_{\mathrm{mod}}}-\overline{u_{\mathrm{obs}}}$ represents the residual between the normalized synthetic and observed wavefields.

The model parameters are updated iteratively using local optimization algorithms, such as the conjugate gradient method (Polyak, 1969). The FWI iteration formula can thus be expressed as follows:

$$m_{n+1} = m_n + \alpha_n d_n \tag{8}$$

$$d_n = \begin{cases} -r_n n = 0 \\ -r_n + \varepsilon_n d_{n-1} n \geq 1 \end{cases} \tag{9}$$

$$\varepsilon_n = \frac{r_n^{\mathrm{T}}(r_n - r_{n-1})}{\|r_{n-1}\|_2^2} \tag{10}$$

Among them, $r = \partial E(m)/\partial m$, ε_n is the correction factor of the Polak-Ribiere method (Schuster, 2017), and its value is calculated according to equation 10; α_n is the step size factor, and this factor can be obtained through the inexact line search method or the exact search method of the parabolic minimum value.

2.2. Implementation Process of Joint Waveform Inversion

The detailed implementation process of the proposed joint inversion method is illustrated in Figure 1, and includes the following steps:

Step 1. Initialization: Set the initial model and the weight factor to 0, and configure n low-pass filters with frequency bands $[0, f_1]$, $[0, f_2]$, $\cdots$, $[0, f_n]$ to implement a multiscale strategy (Yuan et al., 2015) from low to high frequency, where $f_1 < f_2 < \cdots < f_n$.

Step 2. Data preparation and forward modeling: Perform forward modeling to generate synthetic wavefields. Apply the corresponding band-pass filter to both observed and synthetic wavefields, then calculate by the 2D Fourier transform to extract the amplitude spectra.

Step 3. Objective function construction: Calculate the residuals Δu between the normalized observed wavefield and the synthetic wavefield in the x-t domain, and the residuals ΔU of the normalized amplitude spectra in the f-k domain. The weight factor controls the relative contribution of each term.

Step 4. Gradient and step length computation: Compute the gradient of the joint objective function and determine the optimal step length using a suitable optimization method.

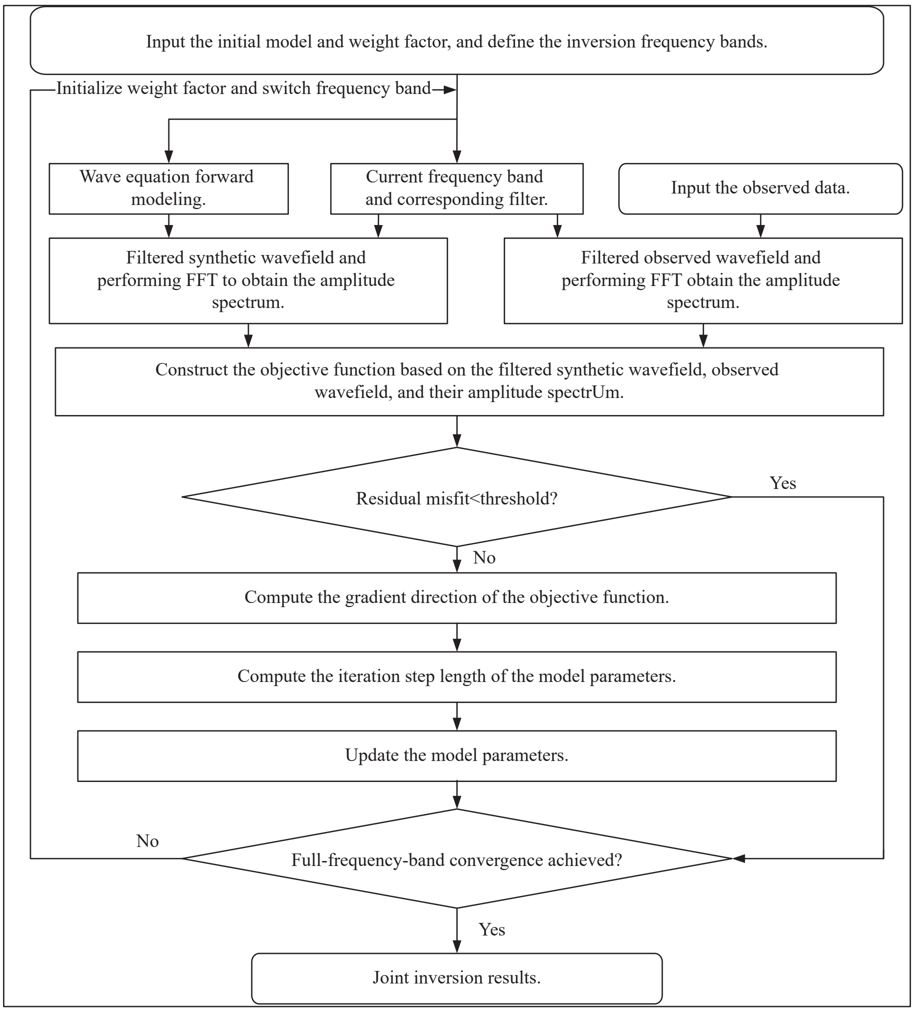

Figure 1. Flowchart of Joint Inversion Implementation.

Step 5. Model update: Update the velocity model parameters accordingly and gradually increase the weight factor, allowing the inversion to transition from amplitude-dominated to waveform-dominated behavior.

Step 6. Frequency band iteration: If the convergence criterion for the current frequency band is satisfied, proceed to the next frequency band using the current model as the starting model and reset the weight factor to 0. If all frequency bands have been completed, output the final inversion result. Otherwise, return to Step 2.

3. Results

In this section, numerical tests are conducted on typical near-surface models to comparatively analyze the performance differences between the joint inversion method, individual waveform inversion, and amplitude spectrum inversion. Finally, the method is applied to actual engineering exploration projects in the loess area to verify its feasibility and practical value.

3.1. Anomalies Model

This test targets two typical types of anomalies commonly encountered in practical exploration: high-velocity anomalies (e.g., boulders, bedrock outcrops) and low-velocity anomalies (e.g., collapsible sinkholes, unconsolidated soil layers). By simulating the geological scenario where both coexist, it verifies the joint inversion method's ability to identify anomalies with different physical properties and its inversion accuracy.

For the anomalies model, the simulation domain size is 60 m × 20 m, with a grid spacing of $\Delta x = \Delta z = 0.5$ m, a recording time of 0.3 s, and a sampling interval of 0.2 ms. The source wavelet is a Ricker wavelet with a dominant frequency of 20 Hz. The receiver spacing is 1 m, with a total of 60 receivers; the shot spacing is 10 m, resulting in 7 shots. Both sources and receivers are deployed linearly along the surface. A free-surface boundary condition is applied at the top, while Convolutional Perfectly Matched Layer (CPML) absorbing boundary conditions are adopted for the left, right, and bottom boundaries of the model, with the absorbing layer consisting of 30 grid points. In the forward modeling process, second-order temporal and tenth-order spatial finite-difference approximations are used. The multi-scale frequency bands are divided into [0,30] Hz and the full frequency band. As shown in Figure 2, the true model is a dual-anomaly model containing one low-velocity anomaly and one high-velocity anomaly. Both anomalies have a size of 5 m × 4 m; the center of the low-velocity anomaly is at (15 m, 10 m), and the center of the high-velocity anomaly is at (45 m, 10 m). The initial model adopts its background medium model. The model parameters are presented in Table 1.

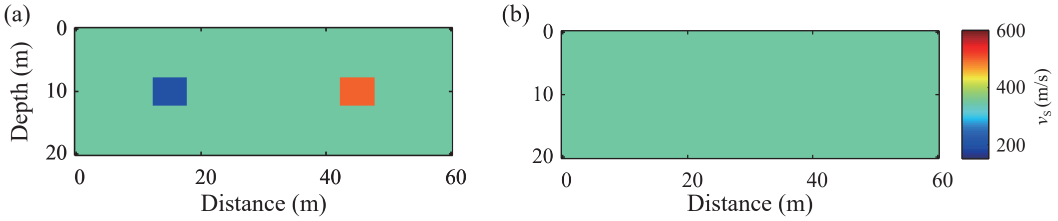

Figure 2. (a) True S-wave velocity model containing anomalies. (b) Initial S-wave velocity model.

Table 1. Model Parameters for the Anomalies Model

Media	v_S (m/s)	v_P (m/s)	ρ (kg/m^3)
Low-velocity anomaly	200	500	2000
High-velocity anomaly	500	1000	2000
Background medium	350	700	2000

After iterative cycles, the inversion results of waveform inversion, amplitude spectrum inversion, and the joint inversion are presented in Figure 3 (with known anomaly zones marked by red rectangles). From the comparison between the three sets of inversion results and the true model, it can be concluded that all three inversion methods can relatively accurately locate the positions of low-velocity and high-velocity anomalies. However, the joint inversion outperforms the individual inversion methods in terms of the inversion accuracy of anomaly size, extent, and velocity parameters. Specifically, the velocity reconstructed by the joint inversion for the high-velocity anomaly is significantly closer to the true shear-wave velocity than those obtained by the individual inversions. Regarding anomaly size, the individual inversion methods generally suffer from the "boundary blurring" issue, whereas the horizontal extent of the anomalies reconstructed by the joint inversion is almost consistent with that of the true model. In addition, both individual inversion methods exhibit artifacts: waveform inversion shows localized high-velocity anomalies exceeding the background velocity beneath the low-velocity bodies, while amplitude spectrum inversion presents similar significant high-velocity distortions. The joint inversion also demonstrates performance here. By synergistically integrating complementary domain information, it effectively mitigates these artificial high-velocity anomalies, with particularly notable improvements in the previously problematic areas beneath the low-velocity anomalies. The reconstructed velocities are all closer to the true shear-wave velocity, which verifies the role of the joint objective function in enhancing the stability and reliability of inversion.

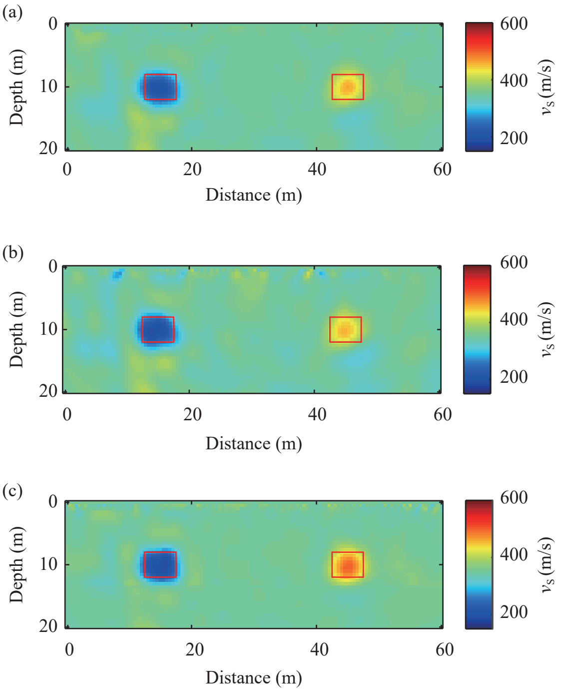

Figure 3. (a) S-wave velocity model obtained from waveform inversion. (b) S-wave velocity model obtained from amplitude spectrum inversion. (c) S-wave velocity model obtained from joint inversion of waveform and amplitude spectrum.

Figure 4 presents the normalized data misfit and model misfit for the three aforementioned inversion methods. The vertical dashed lines mark the frequency band transitions in our multi-scale inversion strategy. The inversion progressively incorporates higher-frequency components to refine the velocity model while maintaining stability and avoiding cycle-skipping. All three methods exhibit good convergence performance. Furthermore, influenced by the amplitude spectrum information, the joint inversion demonstrates higher stability compared to waveform inversion and is less prone to being trapped in local minima. Consequently, it achieves the best performance in terms of model misfit. The model misfit reduction curves correspond well with the inversion results, indicating that the joint inversion outperforms both waveform and amplitude spectrum inversions. Notably, while the data misfits of different inversion methods may appear similar in later iterations, the model misfits reveal significant differences in accuracy. Minimizing data misfit does not guarantee recovery of the correct velocity structure, particularly when the objective function contains multiple local minima. In synthetic tests, the model misfit serves as the definitive metric for evaluating inversion quality. Ultimately, the three methods reduce their normalized model misfits to 0.61, 0.67, and 0.56, respectively (Figure 4 b). Figure 5, using the observed data as a reference, compares the normalized single-trace waveforms and amplitude spectra of the 3rd trace from the 1st shot for the three methods. The extremely high degree of waveform fitting across all three methods indicates good convergence of the optimization algorithms. For clarity, a zoomed-in view of the waveform comparison reveals that the final waveform from the joint inversion is closer to the observed waveform. In the amplitude spectrum comparison, both the amplitude spectrum inversion and joint inversion exhibit a fit that aligns more closely with the observed data. This further demonstrates the superior convergence perform-

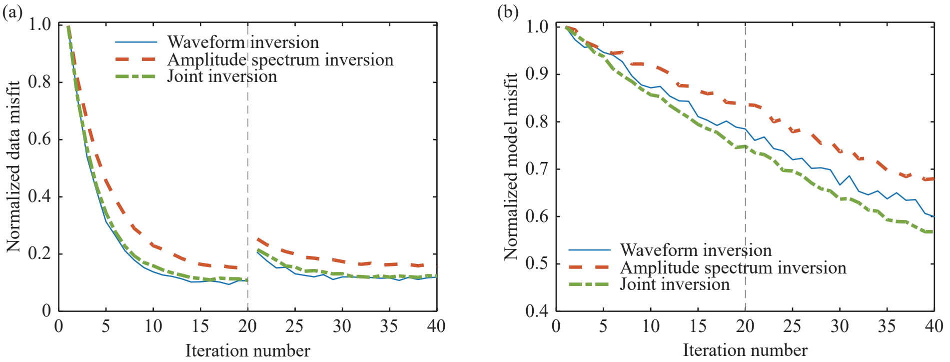

Figure 4. Normalized data misfit curve (a) and model misfit curve (b) for the anomalous body model. The vertical dashed lines indicate the transition points between different frequency stages in the multi-scale inversion strategy.

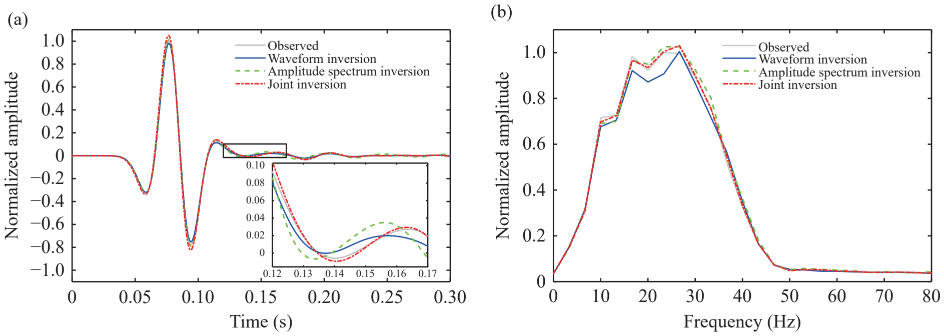

Figure 5. Comparison of normalized (a) waveforms and (b) amplitude spectra for the 3rd trace from the 1st shot. The inset in (a) shows a zoomed-in view from 0.12 s to 0.17 s.

ance and reliability of our joint inversion method.

To further quantify the accuracy differences among the three inversion methods, we extracted a horizontal profile at a depth of z=10 m (intersecting the anomaly centers) and two vertical profiles at horizontal distances of x=15 m and x=45 m (Figure 6). The root-mean-square error (RMSE) between each inverted result and the true model was calculated to precisely determine the accuracy improvements afforded by the joint inversion. For the amplitude spectrum inversion, the RMSE values corresponding to the x=15 m, x=45 m, and z=10 m profiles were 27.91, 34.33, and 27.44 m/s, respectively. For the waveform inversion, the respective RMSE values were 26.99, 33.58, and 27.90 m/s. Conversely, the joint inversion achieved significantly lower RMSE values of 26.20, 26.97, and 22.32 m/s. Compared with the amplitude spectrum inversion, the joint inversion achieved accuracy improvements of 6.13%, 21.44%, and 18.69% across the three profiles, yielding an average improvement of 15.42%. Compared with the waveform inversion, it achieved improvements of 2.94%, 19.68%, and 20.02%, averaging a 14.21% enhancement. Across all analyzed profiles, the joint inversion

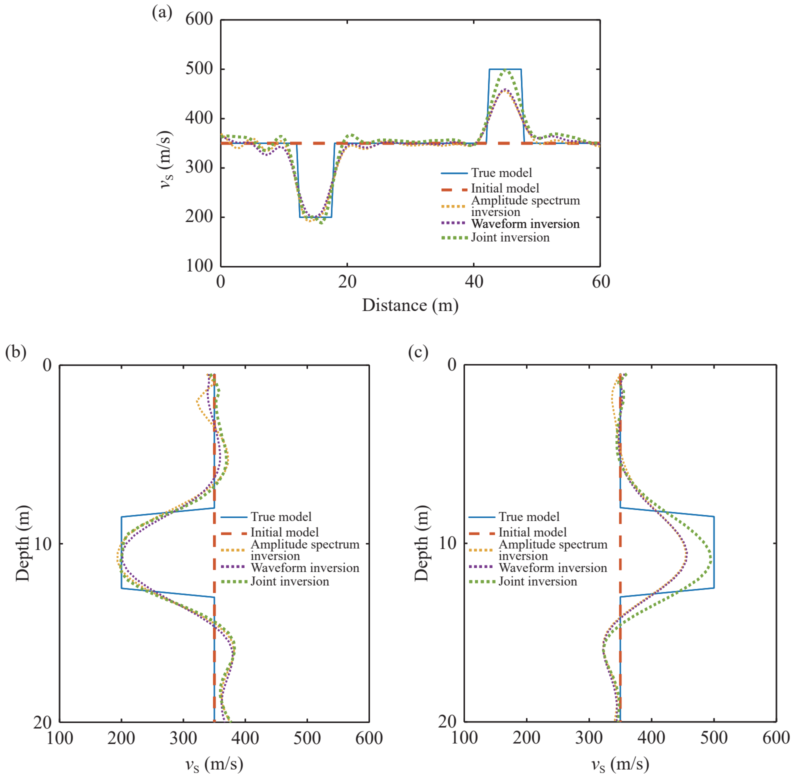

Figure 6. (a) S-wave velocity profile at a depth of 10 m. (b) S-wave velocity profile at a horizontal distance of 15 m. (c) S-wave velocity profile at a horizontal distance of 45 m. Blue solid line: true S-wave velocity; orange dash-dot line: initial S-wave velocity; yellow dotted line: S-wave velocity from amplitude spectrum inversion; purple dotted line: S-wave velocity from waveform inversion; green dotted line: S-wave velocity from joint inversion.

quantitatively outperformed both individual methods. The most substantial improvement was observed in the vertical profile at x=45 m (intersecting the high-velocity anomaly), with error reductions of 21.44% and 19.28% relative to the amplitude spectrum and waveform inversions, respectively. This indicates that the joint inversion exhibits a particularly prominent capability in reconstructing the precise velocity parameters of high-velocity scatterers. Even in the horizontal profile at z=10 m, which simultaneously intersects both anomalies, the joint inversion achieved an accuracy improvement of approximately 20%, verifying its adaptability and reliability in complex, strongly heterogeneous velocity models. Furthermore, the slightly higher average improvement relative to the amplitude spectrum inversion suggests that the multi-domain information fusion effectively compensates for the inherently limited spatial resolution of pure amplitude-based approaches.

3.2. Vertical Fault Model

To verify the method's capability in identifying near-surface structures with lateral physical property discontinuities, a test was conducted using a vertical fault model. The simulation domain of the vertical fault model consists of three layers: the first layer is a low-velocity layer with a thickness of 3 m; the upper interface of the second layer is located at a depth of 6 m on the hanging wall and 12 m on the footwall; the lower interface of the third layer is 11 m away from the hanging wall and 5 m away from the footwall. The parameters for forward and inverse modeling, as well as the acquisition geometry, are consistent with those set for the anomaly model in the previous section. The initial model features a uniform velocity gradient ranging from 250 m/s to 500 m/s. The true model and the initial model are illustrated in Figure 7, and the parameters of the true model are presented in Table 2.

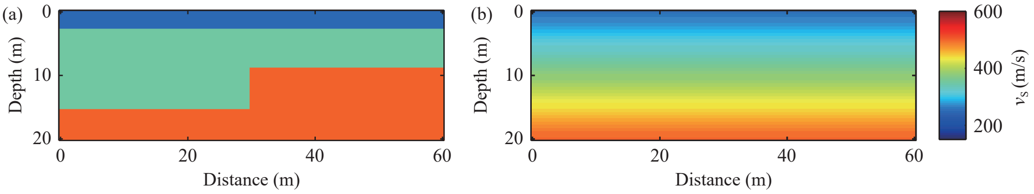

Figure 7. (a) True S-wave velocity model of vertical fault. (b) Initial S-wave velocity model.

Table 2. Model Parameters for the Vertical Fault Model

Layer Index	v_S (m/s)	v_P (m/s)	ρ (kg/m^3)
1	250	500	2000
2	350	700	2000
3	500	1000	2000

After iterative cycles, the inversion results of waveform inversion, amplitude spectrum inversion, and joint inversion are presented in Figure 8, with red dashed lines marking the positions of each layer boundary. A comparison between the aforementioned inversion results and the true model shows that waveform inversion and amplitude spectrum inversion exhibit a certain degree of consistency in identifying basic structural interfaces, realizing relatively accurate recognition of the low-velocity layer interface and the footwall interface of the second layer in the model. The interface morphology and strike derived from these two individual inversion methods are highly consistent with those of the true model, which indicates that both single inversion methods have basic reliability in locating continuous stratigraphic interfaces. Although the two individual methods perform adequately in identifying continuous interfaces, they exhibit distinct shortcomings in resolving the fault zone. Specifically, the delineation of the fault scope remains ambiguous, preventing accurate identification of the fault boundaries. Furthermore, there are notable deviations in characterizing the displacement amplitude of the hanging wall and footwall of the fault. Specifically, in the fault segment at a horizontal distance of 30–40 m in the model, both waveform inversion and amplitude spectrum inversion show slight tilting or broadening, leading to uncertainties in determining the spatial position of the fault. In terms of identifying the hanging wall boundary of the second layer, the accuracy of the two individual inversion methods differs. By utilizing the complete waveform information of seismic waves, waveform inversion can more precisely capture the subtle velocity changes at the hanging wall boundary, resulting in smaller deviations between the strike and undulation of this boundary in the inversion result and those in the true model. In contrast, amplitude spectrum inversion relies solely on amplitude spectrum information and has low sensitivity to velocity gradient changes at the boundary, which leads to local distortion of the hanging wall boundary and lower recognition accuracy compared with waveform inversion. Compared with the two individual inversion methods, the joint inversion fully integrates the sensitivity of waveform inversion to local subtle structures and the stability of amplitude spectrum inversion to macroscopic interfaces. As a result, it achieves more accurate positioning of the true fault position, clearer depiction of each layer interface, and more reliable restoration of velocity values.

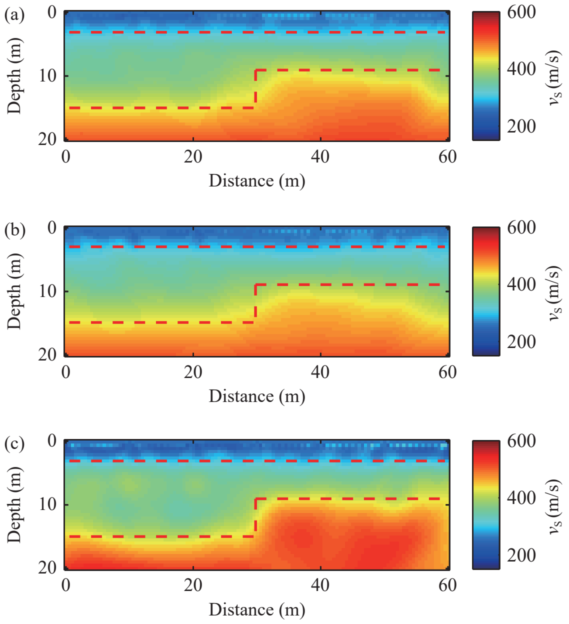

Figure 8. (a) S-wave velocity model obtained from waveform inversion. (b) S-wave velocity model obtained from amplitude spectrum inversion. (c) S-wave velocity model obtained from joint inversion of waveform and amplitude spectrum.

Figure 9 displays the normalized data misfit and model misfit for the three inversion methods. It similarly reflects the characteristics of the joint inversion, namely its relatively fast convergence speed and relatively stable model updates. The final S-wave velocity model error of the joint inversion is reduced to a minimum of 0.61. Figure 10 compares the normalized single-trace waveforms and amplitude spectra of the 20th trace from the 2nd shot for the three methods. The synthetic waveforms and amplitude spectra generated by all three methods maintain good consistency with the observed data in overall shape, verifying the general reliability of the inversion results. However, a careful inspection of the zoomed-in view reveals that the joint inversion achieves the highest degree of agreement with the observed data in terms of phase matching and amplitude, thereby demonstrating the advantages of our proposed method.

To further quantify the accuracy differences among the three inversion methodologies, a rigorous error analysis was performed on the vertical profiles extracted at horizontal distances of x=10 m and x=50 m (Figure 11). For the amplitude spectrum inversion, the RMSE values corresponding to the vertical profiles at x=10 m and x=50 m were 33.85 and 47.85 m/s, respectively. For the waveform inversion, the respective RMSE values were 31.83 and 38.93 m/s. Conversely, the shear-wave velocities derived from the joint inversion yielded significantly lower RMSE values of 30.87 and 34.60 m/s, respectively. Compared with the amplitude spectrum inversion, the joint inversion achieved accuracy improvements of 8.83% and 27.69%, yielding an average improvement of 18.26%. Relative to the waveform inversion, it realized improvements of 3.02% and 11.12%, averaging a 7.07% enhancement. The substantial 18.26% average improvement over the amplitude spectrum inversion indicates that the joint method possesses a significantly superior ability to reconstruct velocities within strongly disturbed fault zones. Furthermore, while the accuracy gap relative to the waveform inversion is smaller, the 7.07% average improvement still endows the joint inversion with a distinct resolution advantage. This demonstrates that while pure waveform inversion is strongly dependent on the initial model and prone to cycle-skipping within complex

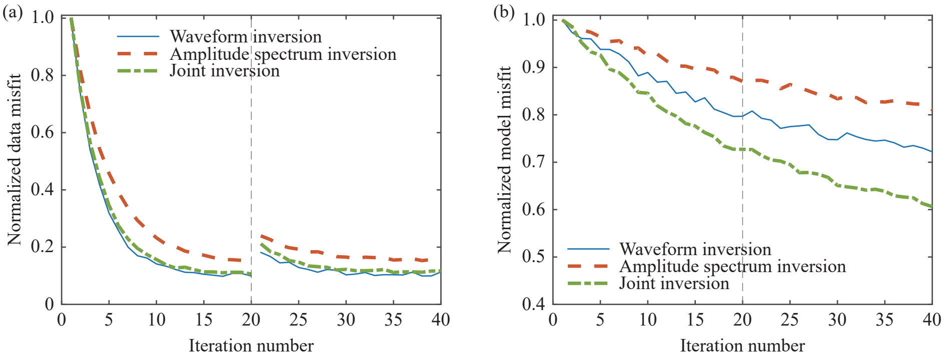

Figure 9. Normalized data misfit curve (a) and model misfit curve (b) for the fault model. The vertical dashed lines indicate the transition points between different frequency stages in the multi-scale inversion strategy.

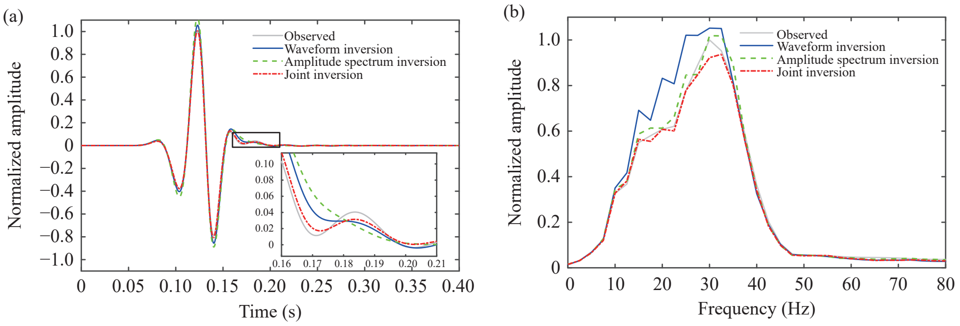

Figure 10. Comparison of normalized (a) waveforms and (b) amplitude spectra for the 20th trace from the 2nd shot. The inset in (a) shows a zoomed-in view from 0.16 s to 0.21 s.

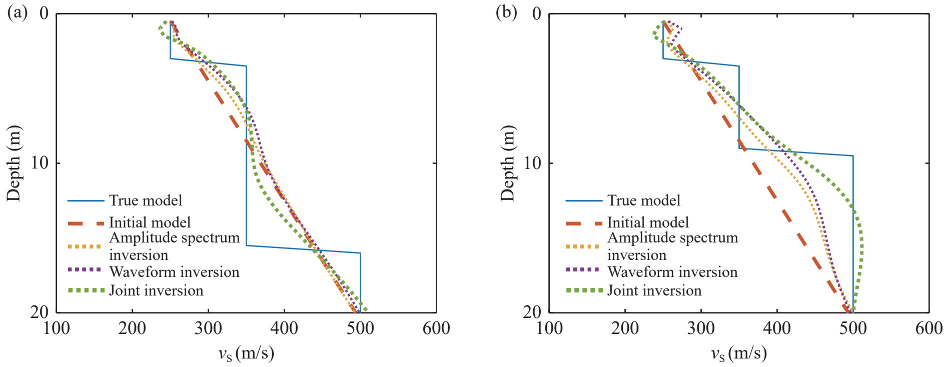

Figure 11. (a) S-wave velocity profile at a horizontal distance of 10 m. (b) S-wave velocity profile at a horizontal distance of 50 m. Blue solid line: true S-wave velocity; orange dash-dot line: initial S-wave velocity; yellow dotted line: S-wave velocity from amplitude spectrum inversion; purple dotted line: S-wave velocity from waveform inversion; green dotted line: S-wave velocity from joint inversion.

fault zones, the amplitude spectrum component of the joint inversion provides robust low-frequency constraints. This integration effectively mitigates instability and significantly enhances the clarity and sharpness of both fault boundaries and stratigraphic interfaces

3.3. Model with a Low-Velocity Interlayer

The simulation domain of the three-layer model containing a low-velocity layer is 40 m × 20 m. The grid spacing is $\Delta x = \Delta z = 0.5$ m, the recording time is 0.3 s, and the sampling interval is 0.2 ms. The source wavelet is a Ricker wavelet with a dominant frequency of 20 Hz. The receiver interval is 1 m, totaling 40 receivers, and the shot interval is 5 m, resulting in 9 shots. The sources and receivers are linearly arranged along the surface at 0.0 m, 5.0 m, 10.0 m, $\cdots$, 35.0 m, and 40.0 m. A free-surface boundary condition is applied at the top, while CPML absorbing boundaries with 30 grid points are set on the left, right, and bottom sides. Second-order temporal and tenth-order spatial finite-difference scheme is employed for forward modeling.

The model is inspired by subsurface geological conditions observed within 20 m depth at a subway construction site in a western city. According to preliminary geotechnical investigations, the 0–4 m layer is compacted fill, the 4–10 m layer is a water-softened low-velocity anomaly, and the 10–20 m layer is a high-velocity stratum. Model parameters such as velocity and density are consistent with real geological data. The initial model features a uniform velocity gradient ranging from 280 m/s to 500 m/s. The parameters of the three-layer low-velocity model are listed in Table 3. The true model and the initial model are illustrated in Figure 12.

Table 3. Model Parameters for a Three-layer Model with a Low-velocity Layer

Layer Index	v_S (m/s)	v_P (m/s)	ρ (kg/m^3)	Layer thickness(m)
1	350	700	2000	4
2	250	500	2000	6
3	500	1000	2000	10

After iterative processing, the results of waveform inversion, amplitude spectrum inversion, and joint inversion are presented in Figure 13, with red dashed lines representing the upper and lower boundaries of the low-

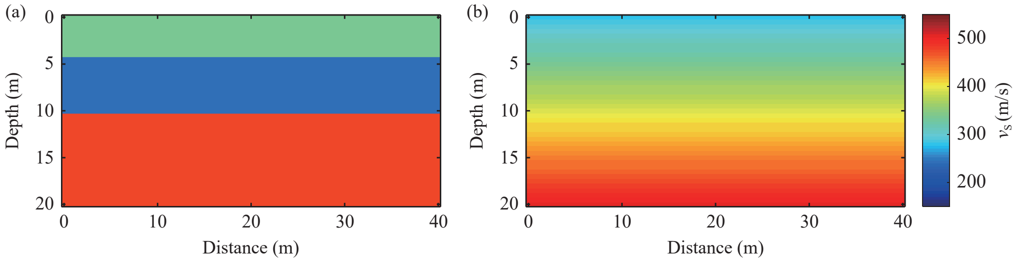

Figure 12. (a) True S-wave velocity model of a three-layer structure containing a low-velocity layer. (b) Initial S-wave velocity model.

velocity interlayer. A comparative analysis of the different inversion results against the true model reveals that all three methods can effectively delineate the velocity discontinuities between strata, verifying their effectiveness in basic horizon identification tasks. When further comparing the detailed accuracy, it is found that the performance of amplitude spectrum inversion is relatively poor— the velocity values of the third layer in its inversion results are much lower than the actual values of the true model. An analysis based on the principle of amplitude spectrum inversion indicates that the core cause of this deviation lies in the fact that amplitude spectrum inversion relies solely on the amplitude information of seismic waves as input data. As seismic waves propagate through the low-velocity soft interlayer, the strong attenuation of high-frequency components results in a severe deficiency of high-frequency information within the amplitude spectrum. Without such high-frequency signals, the amplitude spectrum inversion algorithm significantly underestimates the velocity values of the third layer. Although the results of waveform inversion are superior to those of amplitude spectrum inversion in terms of the clarity of horizon interfaces, they still suffer from local accuracy defects. In the transition zone beneath the low-velocity anomaly model, the inversion results exhibit localized high-velocity anomalies that are inconsistent with the true model. In contrast, the results of joint inversion demonstrate the optimal comprehensive performance. On one hand, it inherits the high-resolution horizon interface identification capability of waveform inversion, enabling accurate differentiation of the three-layer structure (shallow, middle, and deep layers), with the smallest deviation between the spatial positions of each layer interface and those of the true model. On the other hand, by integrating the ability of amplitude spectrum inversion to stably characterize low-frequency velocity trends, the joint inversion effectively remedies the defect of single waveform inversion (which is prone to generating local false anomalies) while supplementing the high-frequency information missing in amplitude spectrum inversion. Ultimately, it achieves high-precision reconstruction of the medium velocity parameters.

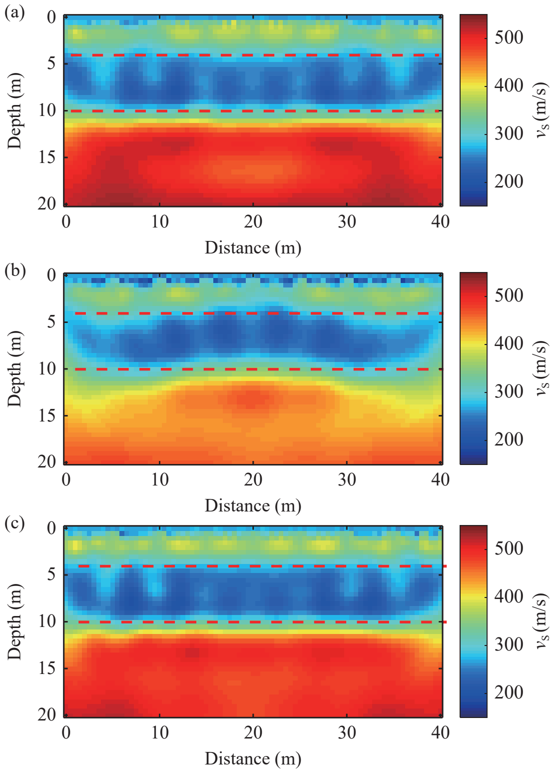

Figure 13. (a) S-wave velocity model obtained from waveform inversion. (b) S-wave velocity model obtained from amplitude spectrum inversion. (c) S-wave velocity model obtained from joint inversion of waveform and amplitude spectrum.

Figure 14 presents the normalized data misfit and model misfit for the three inversion methods. The downward trend of the residuals is similar to that of the two previously mentioned models. The joint inversion possesses a relatively fast convergence speed. In terms of model misfit, the joint inversion converges to the best value of 0.51. Waveform inversion converges to 0.54; both are significantly superior to amplitude spectrum inversion. For the interlayer model, the waveform residual term in the joint inversion plays a relatively significant role. Figure 15 compares the normalized single-trace waveforms and amplitude spectra of the 20th trace from the 5th shot for the three methods. The degree of waveform fitting across the three inversion methods is extremely high, and the zoomed-in view of the waveform comparison shows that the final waveform of the joint inversion is closer to the observed waveform. Although the joint inversion and amplitude spectrum inversion are closer to the observed data in overall trend, the joint inversion and waveform inversion perform better near 20 Hz, which makes a significant contribution to the model resolution.

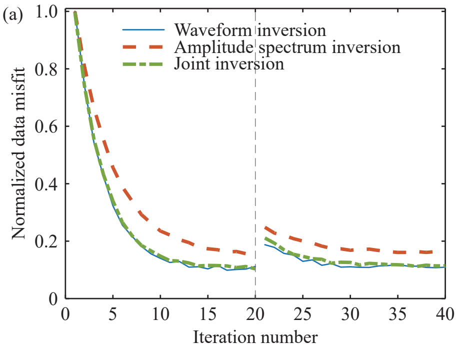

Figure 14. Normalized data misfit curve (a) and model misfit curve (b) for the interlayer model. The vertical dashed lines indicate the transition points between different frequency stages in the multi-scale inversion strategy.

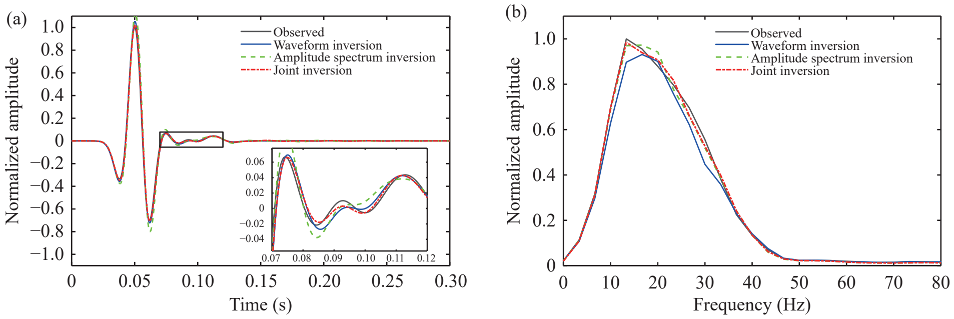

Figure 15. Comparison of normalized (a) waveforms and (b) amplitude spectra for the 20th trace from the 5th shot. The inset in (a) shows a zoomed-in view from 0.07 s to 0.12 s.

Figure 16 compares the vertical shear-wave velocity profiles extracted at horizontal distances of x=10 m and x=25 m against the corresponding true and initial velocities. Quantitative error analysis provides compelling evidence of the proposed method's efficacy. At the x=10 m profile, the joint inversion achieves an RMSE of 34.53 m/s. This represents a remarkable 55.4% reduction relative to the initial model error, corresponding to accuracy improve-

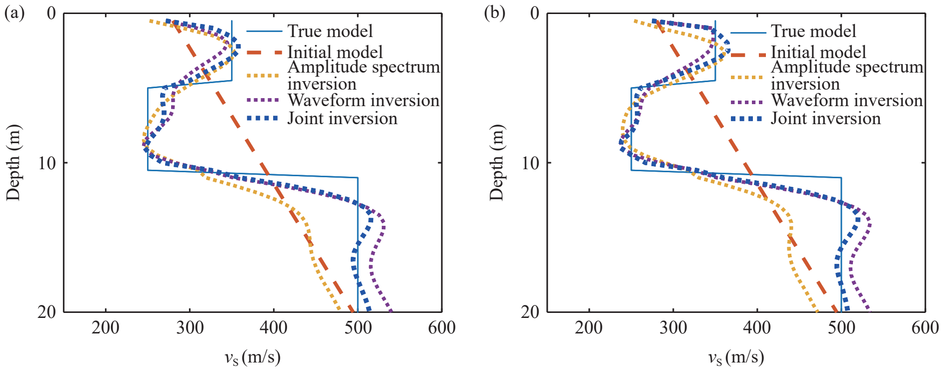

Figure 16. (a) S-wave velocity profile at a horizontal distance of 10 m. (b) S-wave velocity profile at a horizontal distance of 25 m. Blue solid line: true S-wave velocity; orange dash-dot line: initial S-wave velocity; yellow dotted line: S-wave velocity from amplitude spectrum inversion; purple dotted line: S-wave velocity from waveform inversion; blue dotted line: S-wave velocity from joint inversion.

ments of 41.5% and 17.5% over the amplitude spectrum and waveform inversions, respectively. Similarly, at the x=25 m profile, the joint inversion maintains its superiority with an RMSE of 34.65 m/s (compared to the initial error of 77.48 m/s), yielding improvements of 31.9% and 14.6% over the amplitude spectrum and waveform inversions, respectively. While all three methods significantly enhance the accuracy of the initial model, the joint inversion consistently demonstrates optimal convergence characteristics and superior velocity reconstruction across both evaluation locations, whereas the amplitude spectrum inversion yields comparatively weaker results. These findings conclusively validate the enhanced capability of the joint inversion approach in accurately characterizing complex subsurface velocity structures.

The experimental results clearly demonstrate the advantages of the joint inversion approach. Figure 13(c) clearly illustrates the capability of the joint inversion to delineate the boundaries and extent of the low-velocity interlayer, while Figure 16 confirms the agreement between the inverted and true shear-wave velocity fields. Overall, the joint inversion approach effectively circumvents the critical dispersion curve picking step in conventional surface wave methods, thereby mitigating errors arising from dispersion energy ambiguity in low-velocity interlayer models. This comprehensive evaluation suggests that the proposed method offers a practical and accurate solution for reconstructing shear-wave velocity fields in low-velocity interlayer models.

3.4. Analysis of Initial Model Dependence

A fundamental challenge in full-waveform inversion (FWI) utilizing Rayleigh waves is its strong dependence on the accuracy of the initial model, which significantly influences both the convergence trajectory and the final inversion results. Although pure amplitude spectrum inversion can partially mitigate this sensitivity, its inherently limited spatial resolution renders it unsuitable as a standalone benchmark for this analysis. Consequently, we utilize the previously established three-layer low-velocity interlayer model to systematically evaluate and compare the initial model dependence of pure waveform inversion versus the proposed joint inversion.

Three distinct initial models were designed. Init-Model 1 features a shear-wave velocity gradient from 260 m/s to 500 m/s, a compressional-wave velocity gradient from 520 m/s to 1000 m/s, and a density of 2000 kg/m^3. Init-Model 2 has a shear-wave velocity gradient from 300 m/s to 500 m/s, a compressional-wave velocity gradient from 600 m/s to 1000 m/s, and a density of 2000 kg/m^3. Init-Model 3 consists of a shear-wave velocity gradient from 350 m/s to 500 m/s, a compressional-wave velocity gradient from 700 m/s to 1000 m/s, with the same density. The detailed parameters of each initial model are listed in Table 4. The inversion results using waveform inversion and joint inversion under different initial model conditions are illustrated in Figure 17.

Table 4. Parameters of Each Initial Models

	v_S (m/s)	v_P (m/s)	ρ (kg/m^3)
Init-model1	260-500	520-1000	2000
Init-model2	300-500	600-1000	2000
Init-model3	350-500	700-1000	2000

To intuitively assess the influence of different initial models on the inversion performance, 1D vertical profiles comparing the inverted and true shear-wave velocities were extracted at horizontal distances of x=10 m and x=30 m, as shown in Figure 18. From the comparison of the inversion results and velocities of each inversion under various initial model conditions, both methods have a good inversion effect on the thickness of the low-velocity interlayer, and there is a significant difference in the inverted S-wave velocity of the third layer in waveform inversion. In particular, under the condition of the first initial model, the inverted velocity of the third layer is significantly higher than the true S-wave velocity.

Quantitative error analysis explicitly demonstrates the pronounced performance discrepancies between the waveform inversion and the joint inversion frameworks. At the x=10 m profile, the waveform inversion yields RMSE values of 55.91, 43.10, and 38.22 m/s corresponding to Init-models 1, 2, and 3, respectively. This represents significant error reductions of 22.9% and 31.6% as the initial model quality improves. In stark contrast, the joint inversion maintains highly stable RMSE values of 39.43, 38.19, and 40.84 m/s under the identical initial conditions, restricting the performance variation to a mere 7.0%. Similar trends are observed at the x=30 m profile, where the waveform inversion RMSE decreases drastically from 51.56 m/s to 34.07 m/s (a 33.9% reduction) as the initial model improves. Conversely, the joint inversion exhibits minimal fluctuation, with RMSE values tightly constrained between 37.37 m/s and 33.72 m/s (only a 10.8% variation). These quantitative metrics conclusively verify that pure waveform inversion is exceptionally sensitive to the initial model, strictly following the theoretical trend wherein acceptable accuracy is solely predicated on highly accurate starting models. Conversely, the proposed joint inversion method demonstrates superior robustness, exhibiting significantly subdued performance variations across

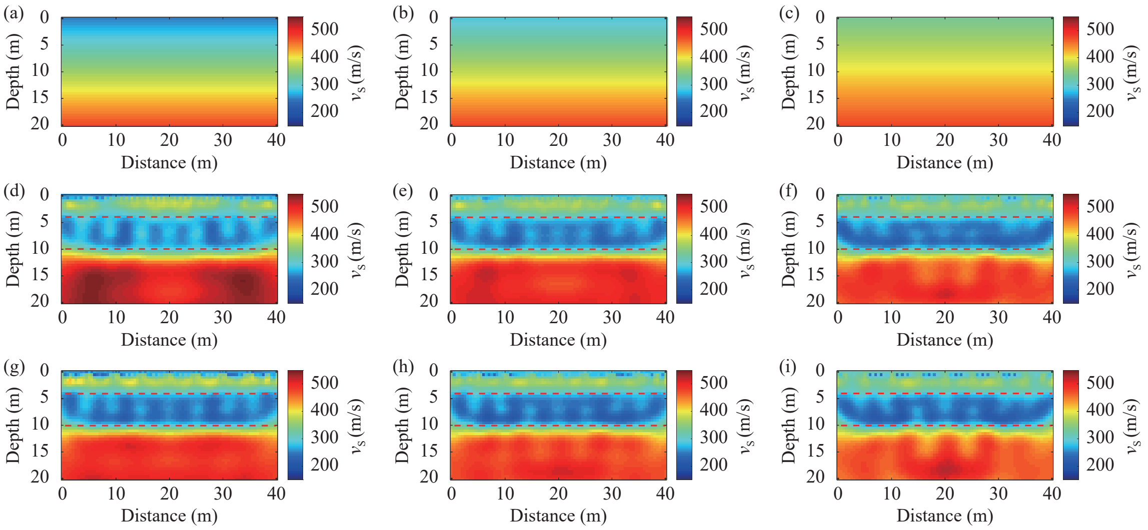

Figure 17. (a) S-wave velocity model of Initial Model 1; (b) S-wave velocity model of Initial Model 2; (c) S-wave velocity model of Initial Model 3; (d) S-wave velocity model from waveform inversion based on Initial Model 1; (e) S-wave velocity model from waveform inversion based on Initial Model 2; (f) S-wave velocity model from waveform inversion based on Initial Model 3; (g) S-wave velocity model from joint inversion based on Initial Model 1; (h) S-wave velocity model from joint inversion based on Initial Model 2; (i) S-wave velocity model from joint inversion based on Initial Model 3.

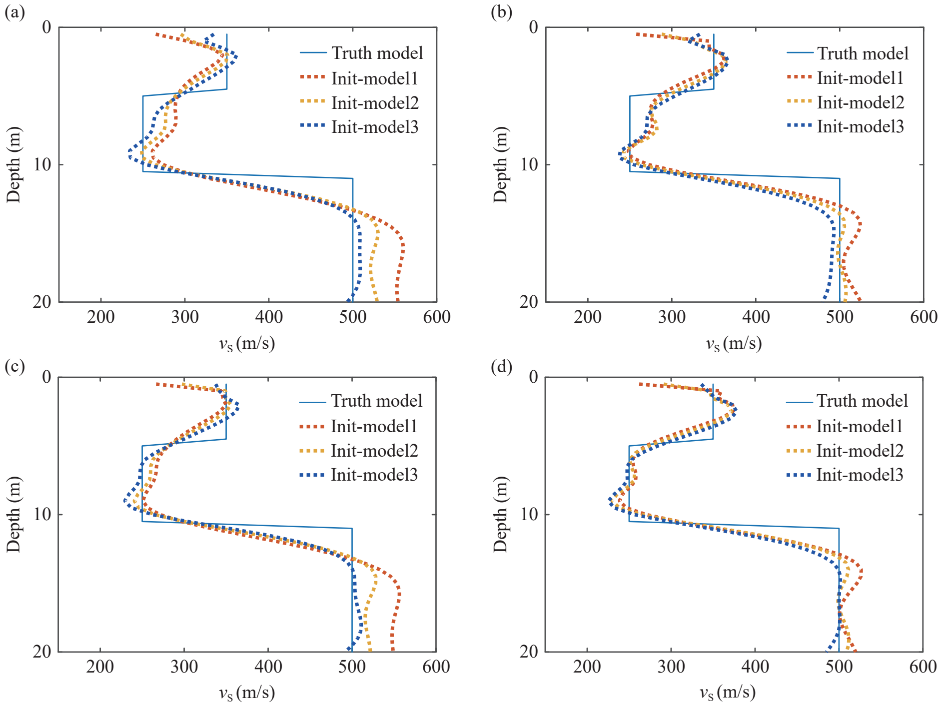

Figure 18. (a) S-wave velocity profile at a horizontal distance of 10 m from waveform inversion; (b) S-wave velocity profile at a horizontal distance of 10 m from joint inversion; (c) S-wave velocity profile at a horizontal distance of 30 m from waveform inversion; (d) S-wave velocity profile at a horizontal distance of 30 m from joint inversion. Blue solid line: true S-wave velocity; orange dotted line: S-wave velocity inverted from Initial Model 1; yellow dotted line: S-wave velocity inverted from Initial Model 2; blue dotted line: S-wave velocity inverted from Initial Model 3.

widely differing initial conditions while maintaining consistently low error levels. This stable convergence behavior confirms the method's drastically reduced dependence on initial model quality, rendering it highly reliable for practical engineering applications where optimal prior models are rarely available.

3.5. Application to 2D Field Data

To validate the practical application of our joint inversion method, we conducted verification studies at an engineering site covered by typical loess deposits in Taibai County, Shaanxi Province, China. The target is a concealed tunnel, representing a typical strong lateral heterogeneity often encountered in loess engineering projects. The survey location and acquisition geometry are illustrated in Figure 19, showing the seismic line deployed along an east-west direction on the platform above the tunnel, perpendicular to the tunnel axis. The known tunnel position extends horizontally from 27 m to 33 m within the survey area, with a vertical depth ranging from 3 m to 6 m.

Figure 19. The survey location and acquisition geometry.

The acquisition system employed 48 receivers with 1 m spacing, positioned from 0 m to 47 m (west to east). Both the sources and receivers were linearly arranged along the surface, with five shot points located at 18.0 m, 24.0 m, 30.0 m, 36.0 m, and 42.0 m respectively. The seismic source consisted of a 15-pound hammer impact, recorded by 4.5 Hz low-frequency geophones at a sampling interval of 0.5 ms for 512 ms record length. During the inversion computation, the model dimensions were set to 48 m × 20 m. To accurately simulate the field source generated by the hammer impact, we employed a damped sine function as the source time function, a method shown to produce synthetic records that closely match actual data (Forbriger, 2004; Wittkamp et al., 2019). Taking into account the significant attenuation of high-frequency energy in the loess medium, a 30 Hz sine-damped source wavelet was used to approximate the actual field source (Figure 20).

Other simulation parameters were configured to match those of the field data acquisition. Free-surface boundary conditions were applied at the top, and CPML absorbing boundaries were implemented at the bottom and lateral sides, with a thickness of 30 grid points. The forward modeling employed a second-order temporal and tenth-order spatial finite-difference scheme to ensure numerical accuracy and stability.

Prior to inversion, we first performed essential preprocessing including dead trace removal and high-frequency random noise suppression. Figure 21 displays the preprocessed shot gathers acquired at 30 m and 36 m field positions, which represent partial observation data used for subsequent inversion.

The dispersion curves extracted via phase-shift method (Park et al., 2007) initially indicate an S-wave velocity range of 200-500 m/s for the survey area (Figure 22). Based on regional geological data with a typical Poisson's ratio of 0.44, we estimated P-wave velocities between 600-1500 m/s and fixed the density at 1900 kg/m^3. Figure 22 (b) presents the initial S-wave velocity model with a uniform gradient increase from 200 m/s to 500 m/s within 0-20 m depth.

To enhance solution stability and avoid local minima, we implemented a multi-scale inversion strategy with

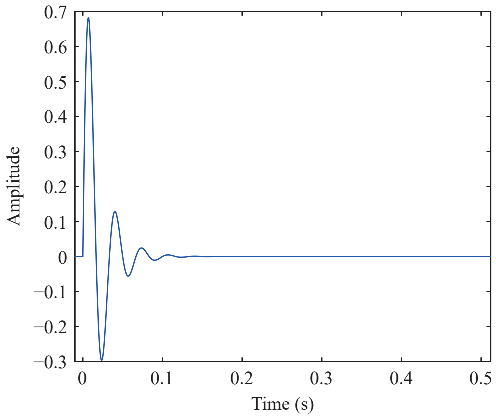

Figure 20. The estimated source wavelet used in the field data inversion.

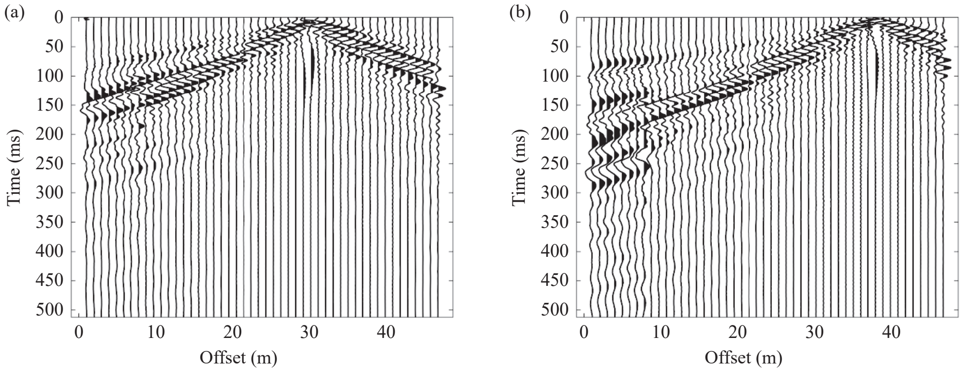

Figure 21. The preprocessed shot gathers acquired at 30 m (a) and 36 m (b) field positions.

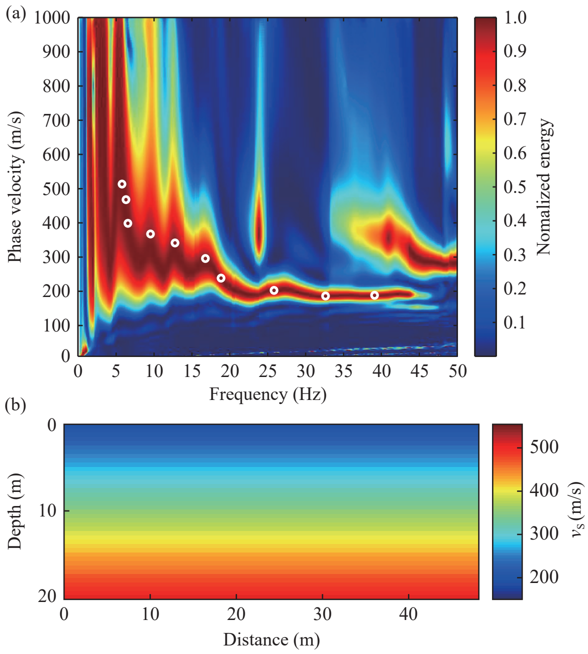

Figure 22. (a)Frequency-velocity image (dispersion image) with the manually picked dispersion curve (solid dots) by following the peaks at different frequencies.(b) Initial S-wave velocity model.

progressively wider frequency bands: [5-30] Hz and the full frequency band. Figure 23 displays the S-wave velocity inversion results obtained using the three different methods, where the red rectangle accurately marks the actual tunnel location. To verify the effectiveness of the proposed method, we compared the joint inversion results with those from individual inversions. Due to the strong scattering and attenuation characteristics of the loess medium, the individual waveform inversion is prone to trapping in local minima, leading to obvious artifacts and blurred boundaries in the final model. Conversely, while the individual amplitude spectrum inversion successfully recovers the background velocity trend, it suffers from limited resolution and cannot precisely constrain the geometry of the anomaly. In contrast, the joint inversion significantly improves imaging quality. As shown in Figure 23(c), the joint inversion results indicate a clear stratification interface at approximately 10 m depth, consistent with known geological conditions. Additionally, a low-velocity anomaly was identified within the horizontal range of 26–34 m and the depth range of 3–7 m, closely matching the known position of the tunnel. The inversion successfully delineates the tunnel location, accurately capturing the depth of the tunnel roof and slightly overestimating the bottom depth. Overall, for the loess area, this method yields a high-resolution image of the subsurface structure at the engineering scale and thus demonstrates promising applicability for practical tunnel detection in this geologically distinctive region.

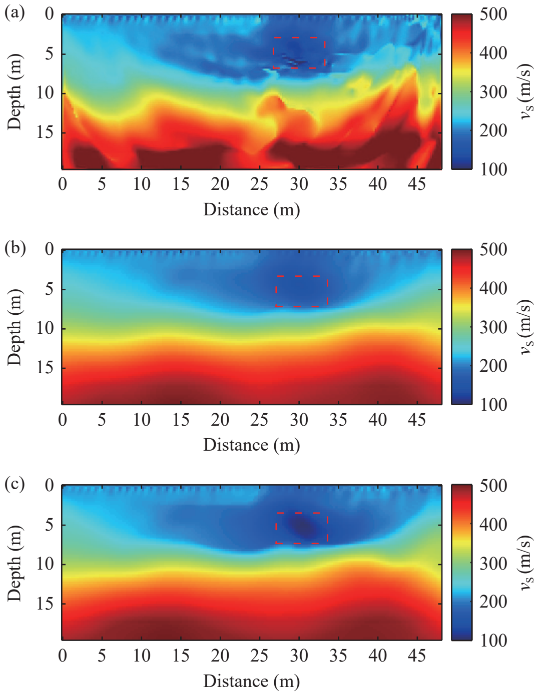

Figure 23. (a) S-wave velocity model obtained from waveform inversion. (b) S-wave velocity model obtained from amplitude spectrum inversion. (c) S-wave velocity model obtained from joint inversion of waveform and amplitude spectrum.

The normalized data misfit for the field data is shown in Figure 24. The normalized objective function value drops to approximately 0.55. Considering the influence of noise, formation attenuation, and parameter crosstalk in the data, this error value is acceptable. To comprehensively evaluate the data fitting quality across different inversion methods, Figure 25 presents the 3rd shot gather comparisons between the observed field data and the modeled synthetic data from different velocity models. The initial smoothed gradient model shows poor fit to the observed data, with significant phase mismatches and amplitude discrepancies. In contrast, the joint inversion achieves exceptional waveform matching throughout the entire shot gather, with both phase and amplitude well reproduced across all offsets. The waveform inversion and amplitude spectrum inversion show intermediate fitting quality, better than the initial model but inferior to the joint approach. These comparisons confirm that the joint inversion effectively combines the global convergence of amplitude spectrum inversion with the high-resolution imaging capabilities of waveform inversion, achieving superior data fitting. Figure 26 compares the normalized single-trace waveforms and amplitude spectra of the 20th trace from the 3rd shot for the three methods. The complexity of shallow near-surface media results in a certain degree of fitting residual remaining in the seismic traces. However, the fitting of the waveforms and amplitude spectra from the joint inversion with the observed data is generally good, thereby ensuring the reliability of the final inversion results. These results strongly demonstrate that the proposed joint inversion method possesses significant engineering practical value.

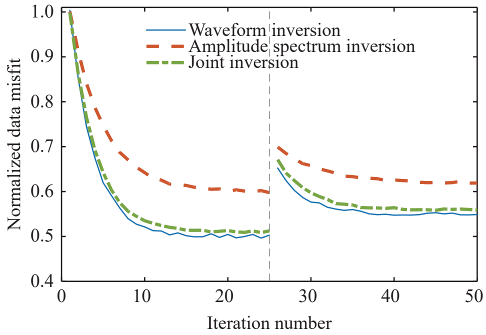

Figure 24. Normalized data misfit curve. The vertical dashed lines indicate the transition points between different frequency stages in the multi-scale inversion strategy.

4. Discussion

The joint inversion method of Rayleigh wave waveform and amplitude spectrum proposed in this study

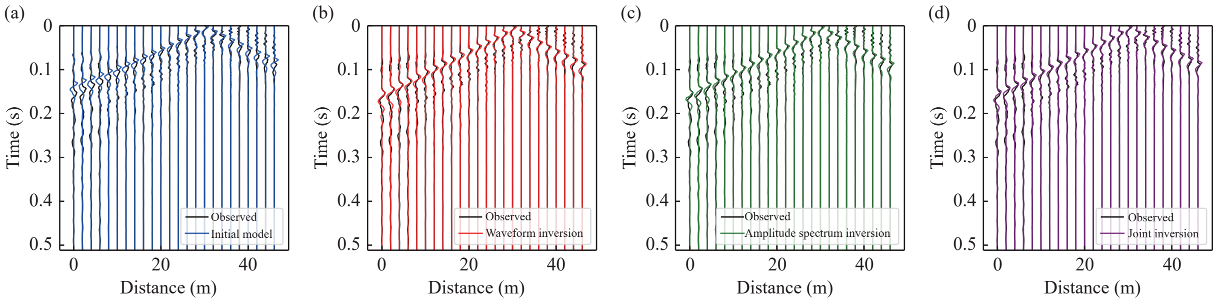

Figure 25. Shot gather comparison between observed data and modeled data from different inversion methods for the field dataset (shot 3). (a) Initial model vs. observed data. (b) Waveform inversion result vs. observed data. (c) Amplitude spectrum inversion result vs. observed data. (d) Joint inversion result vs. observed data.

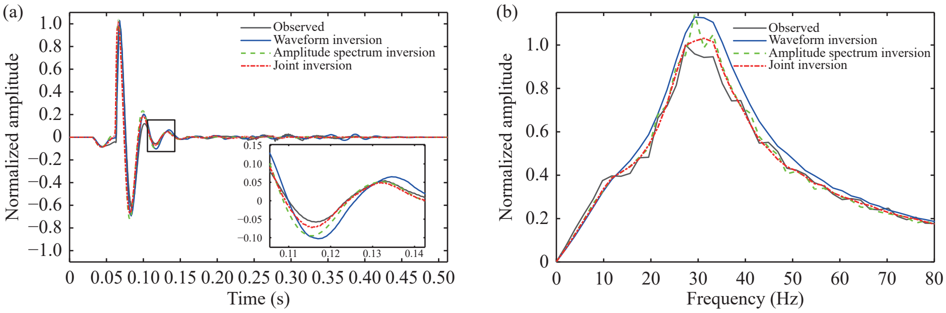

Figure 26. Comparison of normalized (a) waveforms and (b) amplitude spectra for the 20th trace from the 3rd shot. The inset in (a) shows a zoomed-in view from 0.105 s to 0.145 s.

exhibits distinct advantages for near-surface exploration in loess areas, both in terms of theoretical mechanism and engineering practice. Through systematic model tests and field data verification, the core value and application characteristics of this method can be analyzed in depth. The core value of the joint inversion method lies in the synergistic integration of the advantages of amplitude spectrum inversion and waveform inversion through a dynamically weighted joint objective function. Through carefully designed weighting coefficients, priority is given to the amplitude spectrum component in the early stage of iteration. Compared to pure FWI, this strategy exhibits reduced dependence on the accuracy of the source wavelet. Studies have shown that the frequency limit for the initial model in amplitude-based inversion is much more relaxed (Pérez et al., 2014). Therefore, even with slight deviations in the estimated source wavelet, the amplitude spectrum helps constrain the model to the correct background velocity structure. The amplitude spectrum inversion component helps avoid cycle-skipping issues while constructing a geologically reasonable initial velocity model. Subsequently, waveform information gradually dominates the inversion process to generate high-resolution model updates. This iterative approach compensates for the shortcomings of individual inversion methods: it not only addresses the insufficient resolution of amplitude spectrum inversion caused by its neglect of high-frequency information but also overcomes the drawbacks of waveform inversion, such as strong dependence on the initial model and susceptibility to converging to local minima.

Despite these advantages, the proposed methodology presents certain limitations that warrant further optimization. The simultaneous computation of time-domain wavefields and f-k domain amplitude spectra inherently imposes a high computational burden. Without further algorithmic optimization, this computational cost may currently restrict its widespread application in massive, large-scale exploration scenarios within loess areas. Future research will focus on three primary directions: First, improving overall computational efficiency through advanced parallel computing technologies and GPU acceleration; Second, extending the current 2D elastic method to three-dimensional (3D) viscoelastic media to more accurately simulate the severe attenuation and complex propagation characteristics of Rayleigh waves in porous loess; Third, conducting extensive field verifications across diverse engineering scenarios in loess regions — such as landslide slip-surface detection and foundation liquefaction risk assessment —to further validate the universality and practical reliability of the method.

5. Conclusions

This study proposed a joint inversion method integrating Rayleigh wave waveform and amplitude spectrum. By fusing the advantages of the two inversion techniques through a dynamically weighted joint objective function, this method effectively mitigates the core issues of conventional Rayleigh wave inversion in loess area near-surface exploration, including limited lateral resolution, strong dependence on initial models, and proneness to converging to local minima. Verified by numerical simulations, in typical loess area models (anomaly body, fault, and low-velocity interlayer models), the method achieves an accuracy improvement of 14 to 18 percent compared with individual waveform inversion or amplitude spectrum inversion. It enables precise characterization of the boundaries and velocity parameters of concealed geological features such as collapsible voids and fault interfaces. Through the low-frequency constraints provided by amplitude spectrum inversion, the joint inversion significantly reduces its reliance on initial models, alleviating the challenge of acquiring accurate initial models in loess areas. When the shear-wave velocity of the initial model varies, the fluctuation of its RMSE is only 7.0 percent. This is substantially lower than the 31.6 percent RMSE variation observed in conventional waveform inversion, demonstrating exceptional stability. For the field application of tunnel exploration in the loess area of Shaanxi Province, the method achieved high-precision imaging of near-surface structures within a 20 m depth range. It further succeeds in delineating stratigraphic interfaces and locating concealed defects, thereby offering reliable technical support for engineering safety assessment.

Acknowledgments

This work was supported by the National Natural Science Foundation of China (42174176, 42574205, 42104051) and the National Key Research and Development Program (2021YFA0716902).

Conflict of interest

The authors affirm that they have no financial and personal relationships with any individuals or organization that could have potentially influenced the work presented in this paper.

References

Borisov D, Modrak R, Gao FC and Tromp J (2018). 3D elastic full-waveform inversion of surface waves in the presence of irregular topography using an envelope-based misfit function. Geophysics **83**(1): R1–R11. https://doi.org/10.1190/geo2017-0081.1.

Bunks C, Saleck FM, Zaleski S and Chavent G (1995). Multiscale seismic waveform inversion. Geophysics **60**(5): 1457–1473. https://doi.org/10.1190/1.1443880.

Chang WS, Shao GZ, Wu H, Huo KY, Wang Z, Zhao RF, Liu XSR and Zhu HX (2025). Improving the retrieval of empirical green's function using adaptive covariance filter and weighted stacking. IEEE Trans Geosci Remote Sens **63**: 5909416. https://doi.org/10.1109/TGRS.2025.3555221.

Chen YQ and Saygin E (2022). 3‑D *S* wave imaging via robust neural network interpolation of 2‑D profiles from wave-equation dispersion inversion of seismic ambient noise. J Geophys Res Solid Earth **127**(12): e2022JB024663. https://doi.org/10.1029/2022JB024663.

Dal Moro G, Moura RMM and Moustafa SSR (2015). Multi-component joint analysis of surface waves. J Appl Geophys **119**: 128–138. https://doi.org/10.1016/j.jappgeo.2015.05.014.

Espin I, Salaun N, Jiang H and Reinier M (2023). From FWI to ultra-high-resolution imaging. Leading Edge **42**(1): 16–23. https://doi.org/10.1190/tle42010016.1.

Fichtner A, Thrastarson S, van Herwaarden DP and Noe S (2024). An illustrated guide to: parsimonious multi-scale full-waveform inversion. Earthq Sci **37**(6): 574–583. https://doi.org/10.1016/j.eqs.2024.07.004.

Forbriger T (2004). Dynamics of the hammer blow. Mitteilungen **1**: 93–97. **(查阅网上资料, 未能确认本条文献修改是否正确, 请确认)**.

Gao LL, Pan YD, Rieder A, Bohlen T and Mao WJ (2023). Multiparameter 2-D viscoelastic full-waveform inversion of Rayleigh waves: a field experiment at Krauthausen test site. Geophys J Int **234**(1): 297–312. https://doi.org/10.1093/gji/ggad072.

Groos L, Schäfer M, Forbriger T and Bohlen T (2017). Application of a complete workflow for 2D elastic full-waveform inversion to recorded shallow-seismic Rayleigh waves. Geophysics **82**(2): R109–R117. https://doi.org/10.1190/geo2016-0284.1.

Hu Y, Fu LY, Li QQ, Deng WB and Han LG (2022). Frequency-wavenumber domain elastic full waveform inversion with a multistage phase correction. Remote Sens **14**(23): 5916. https://doi.org/10.3390/rs14235916.

Huo KY, Shao GZ, Wang GS, Bai S and Wu H (2023). Numerical simulation and dispersion curve verification of three-dimensional background noises. Oil Geophys Prospect **58**(4): 847–856. https://doi.org/10.13810/j.cnki.issn.1000-7210.2023.04.010 (in Chinese with English abstract).

Huo YY, Yang R, Pan JS and Li X (2024). A 3D surface wave attenuation method based on dispersion curve analysis and its application. Acta Geophys **72**(6): 4123–4138. https://doi.org/10.1007/s11600-024-01318-2.

Lamuraglia S, Stucchi E and Aleardi M (2023). Application of a global–local full‑waveform inversion of Rayleigh wave to estimate the near‑surface shear wave velocity model. Near Surf Geophys **21**(1): 21–38. https://doi.org/10.1002/nsg.12243.

Le Z, Song XH, Zhang XQ, Shen C, Ai HB, Yuan SC and Fu DG (2024). Particle swarm optimization for Rayleigh wave frequency-velocity spectrum inversion. J Appl Geophys **222**: 105311. https://doi.org/10.1016/j.jappgeo.2024.105311.

Li J, Dutta G and Schuster G (2017). Wave-equation Q_s inversion of skeletonized surface waves. Geophys J Int **209**(2): 979–991. https://doi.org/10.1093/gji/ggx051.

Li J, Hanafy S, Liu ZL and Schuster GT (2019a). Wave-equation dispersion inversion of Love waves. Geophysics **84**(5): R693–R705. https://doi.org/10.1190/geo2018-0039.1.

Li J, Lin FC, Allam A, Ben-Zion Y, Liu ZL and Schuster G (2019b). Wave equation dispersion inversion of surface waves recorded on irregular topography. Geophys J Int **217**(1): 346–360. https://doi.org/10.1093/gji/ggz005.

Long GH, Li XF, Zhang MG and Zhu T (2009). Visco-acoustic transmission waveform inversion of velocity structure in space-frequency domain. Earthq Sci **22**(1): 45–52. https://doi.org/10.1007/s11589-009-0045-y.

Masoni I, Brossier R, Virieux J and Boelle JL (2014). Robust full waveform inversion of surface waves. In: SEG Technical Program Expanded Abstracts 2014. Washington: SEG, 1126–1130. https://doi.org/10.1190/segam2014-1077.1.

Mi BB, Xia JH, Shen C, Wang LM, Hu Y and Cheng F (2017). Horizontal resolution of multichannel analysis of surface waves. Geophysics **82**(3): EN51–EN66. https://doi.org/10.1190/geo2016-0202.1.

Operto S, Gholami A, Aghamiry H, Guo GS, Beller S, Aghazade K, Mamfoumbi F, Combe L and Ribodetti A (2023). Extending the search space of full-waveform inversion beyond the single-scattering Born approximation: a tutorial review. Geophysics **88**(6): R671–R702. https://doi.org/10.1190/geo2022-0758.1.

Pan WY and Innanen KA (2019). Amplitude-based misfit functions in viscoelastic full-waveform inversion applied to walk-away vertical seismic profile data. Geophysics **84**(5): B335–B351. https://doi.org/10.1190/geo2018-0765.1.

Pan YD, Xia JH, Xu YX, Gao LL and Xu ZB (2016). Love-wave waveform inversion in time domain for shallow shear-wave velocity. Geophysics **81**(1): R1–R14. https://doi.org/10.1190/geo2014-0225.1.

Pan YD, Gao LL and Bohlen T (2018). Time-domain full-waveform inversion of Rayleigh and Love waves in presence of free-surface topography. J Appl Geophys **152**: 77–85. https://doi.org/10.1016/j.jappgeo.2018.03.006.

Pan YD, Gao LL and Bohlen T (2019). High-resolution characterization of near-surface structures by surface-wave inversions: from dispersion curve to full waveform. Surv Geophys **40**(2): 167–195. https://doi.org/10.1007/s10712-019-09508-0.

Pan YD, Gao LL and Bohlen T (2021). Random-objective waveform inversion of 3D‐9C shallow-seismic field data. J Geophys Res Solid Earth **126**(9): e2021JB022036. https://doi.org/10.1029/2021JB022036.

Pan YD and Gao LL (2023). Individual and joint inversions of shallow-seismic Rayleigh and love waves: full-waveform inversion versus random-objective waveform inversion. Surv Geophys **44**(4): 983–1008. https://doi.org/10.1007/s10712-023-09775-y.

Park C (2013). MASW for geotechnical site investigation. Leading Edge **32**(6): 656–662. https://doi.org/10.1190/tle32060656.1.

Park CB, Miller RD and Xia JH (1999). Multichannel analysis of surface waves. Geophysics **64**(3): 800–808. https://doi.org/10.1190/1.1444590.

Park CB, Miller RD, Xia JH and Ivanov J (2007). Multichannel analysis of surface waves (MASW) —active and passive methods. Leading Edge **26**(1): 60–64. https://doi.org/10.1190/1.2431832.

Pérez Solano CA, Donno D and Chauris H (2014). Alternative waveform inversion for surface wave analysis in 2-D media. Geophys J Int **198**(3): 1359–1372. https://doi.org/10.1093/gji/ggu211.

Plessix RE (2006). A review of the adjoint-state method for computing the gradient of a functional with geophysical applications. Geophys J Int **167**(2): 495–503. https://doi.org/10.1111/j.1365-246X.2006.02978.x.

Polyak BT (1969). The conjugate gradient method in extremal problems. USSR Comput Math Math Phys **9**(4): 94–112. https://doi.org/10.1016/0041-5553(69)90035-4.

Schuster GT (2017). Seismic Inversion. Society of Exploration Geophysicists, Tulsa. https://doi.org/10.1190/1.9781560803423.

Socco LV, Foti S and Boiero D (2010). Surface-wave analysis for building near-surface velocity models — Established approaches and new perspectives. Geophysics **75**(5): 75A83–75A102. https://doi.org/10.1190/1.3479491.

Song C, Wang YH, Richardson A and Liu C (2023). Weighted envelope correlation-based waveform inversion using automatic differentiation. IEEE Trans Geosci Remote Sensing **61**: 4505011. https://doi.org/10.1109/TGRS.2023.3300127.

Song ZH, Zeng XF and Thurber CH (2021). Surface-wave dispersion spectrum inversion method applied to Love and Rayleigh waves recorded by distributed acoustic sensing. Geophysics **86**(1): EN1–EN12. https://doi.org/10.1190/geo2019-0691.1.

Tarantola A (1984). Inversion of seismic reflection data in the acoustic approximation. Geophysics **49**(8): 1259–1266. https://doi.org/10.1190/1.1441754.

Tohti M, Liu JH, Xiao WJ, Wang YB, Di QY and Zhou KF (2022). Full‐waveform inversion of surface waves based on instantaneous‐phase coherency. Near Surf Geophys **20**(5): 494–506. https://doi.org/10.1002/nsg.12229.

Tran KT and Hiltunen DR (2012). One-dimensional inversion of full waveforms using a genetic algorithm. J Environ Eng Geophys **17**(4): 197–213. https://doi.org/10.2113/JEEG17.4.197.

Tran KT and McVay M (2012). Site characterization using Gauss–Newton inversion of 2-D full seismic waveform in the time domain. Soil Dyn Earthq Eng **43**: 16–24. https://doi.org/10.1016/j.soildyn.2012.07.004.

Virieux J and Operto S (2009). An overview of full-waveform inversion in exploration geophysics. Geophysics **74**(6): WCC1–WCC26. https://doi.org/10.1190/1.3238367.

Wang CF, Zhang J, Yan LH, Liu H and Zhao D (2014). Application of passive source surface-wave method in site engineering seismic survey. Earthq Sci **27**(1): 101–106. https://doi.org/10.1007/s11589-014-0065-0.

Wang J and Yan YF (2021). The high-speed inversion of Rayleigh wave and its microtremor application analysis. IEEE Access **9**: 41397–41406. https://doi.org/10.1109/ACCESS.2021.3064693.

Wang XN, Zhang J, Guo CA, Zhao S and Cheng H (2022). Seismic interferometry in linear radon domain applying to noise passive data. IEEE Geosci Remote Sensing Lett **19**: 7504205. https://doi.org/10.1109/LGRS.2021.3088141.

Weemstra C, Boschi L, Goertz A and Artman B (2013). Seismic attenuation from recordings of ambient noise. Geophysics **78**(1): Q1–Q14. https://doi.org/10.1190/geo2012-0132.1.

Wittkamp F, Athanasopoulos N and Bohlen T (2019). Individual and joint 2-D elastic full-waveform inversion of Rayleigh and Love waves. Geophys J Int **216**(1): 350–364. https://doi.org/10.1093/gji/ggy432.

Woods RD (1968). Screening of surface wave in soils. J Soil Mech Found Div **94**(4): 951–979. https://doi.org/10.1061/JSFEAQ.0001180.

Wu YH, Pan SL, Yi SB, Chen JY, Cui QH and Song GJ (2023). An automatic screening method for the passive surface-wave imaging based on the F–K domain energy characteristics. IEEE Trans Geosci Remote Sens **61**: 5920112. https://doi.org/10.1109/TGRS.2023.3321786.

Xie C, Qin ZL, Wang JH, Song P, Shen HG, Yu SQ, Ma BJ and Liu XQ (2024). Full waveform inversion based on hybrid gradient. Pet Sci **21**(3): 1660–1670. https://doi.org/10.1016/j.petsci.2024.01.013.

Xue YH, Dong ZQ, Li G, Yu DH, Wang R and Zhang H (2024). Multi‐mode inversion of dispersive surface‐wave free fields in layered media. Earthq Eng Struct Dyn **53**(7): 2331–2353. https://doi.org/10.1002/eqe.4120.

Yilmaz Ö, Gao K, Delic M, Xia JH, Huang LJ, Jodeiri H and Pugin A (2022). A reality check on full-wave inversion applied to land seismic data for near-surface modeling. Leading Edge **41**(1): 40–46. https://doi.org/10.1190/tle41010040.1.

Yuan YO, Simons FJ and Bozdağ E (2015). Multiscale adjoint waveform tomography for surface and body waves. Geophysics **80**(5): R281–R302. https://doi.org/10.1190/geo2014-0461.1.

Zeng C, Xia JH, Miller RD and Tsoflias GP (2011). Feasibility of waveform inversion of Rayleigh waves for shallow shear-wave velocity using a genetic algorithm. J Appl Geophys **75**(4): 648–655. https://doi.org/10.1016/j.jappgeo.2011.09.028.

Zhang ZD, Alajami M and Alkhalifah T (2020). Wave-equation dispersion spectrum inversion for near-surface characterization using fibre-optics acquisition. Geophys J Int **222**(2): 907–918. https://doi.org/10.1093/gji/ggaa211.

Zhang ZD, Saygin E, He LY and Alkhalifah T (2021). Rayleigh wave dispersion spectrum inversion across scales. Surv Geophys **42**(6): 1281–1303. https://doi.org/10.1007/s10712-021-09667-z.

Zhang ZD, Alkhalifah T and Liu YK (2024). Full dispersion-spectrum inversion of surface waves. J Geophys Res Solid Earth **129**(6): e2023JB028469. https://doi.org/10.1029/2023JB028469.